



PAPER • OPEN ACCESS

Cancer cell migration depends on adjacent ASC and adipose spheroids in a 3D bioprinted breast cancer model

To cite this article: Hannes Horder *et al* 2024 *Biofabrication* **16** 035031

View the [article online](#) for updates and enhancements.

You may also like

- [Vascularized adipose tissue engineering: moving towards soft tissue reconstruction](#)
Arne Peirsman, Huu Tuan Nguyen, Michiel Van Waeyenberge et al.
- [The development of a high throughput drug-responsive model of white adipose tissue comprising adipogenic 3T3-L1 cells in a 3D matrix](#)
Alexander D Graham, Rajesh Pandey, Viktoriya S Tsancheva et al.
- [Xenogenic induction of adipose tissue and maintenance through pre- and post-conditioning using external volume expansion](#)
Mengfan Wu, Dany Y Matar, Zhen Yu et al.

Biofabrication



PAPER

OPEN ACCESS

RECEIVED
14 January 2024

REVISED
22 April 2024

ACCEPTED FOR PUBLICATION
13 June 2024

PUBLISHED
27 June 2024

Original content from this work may be used under the terms of the [Creative Commons Attribution 4.0 licence](#).

Any further distribution of this work must maintain attribution to the author(s) and the title of the work, journal citation and DOI.



Cancer cell migration depends on adjacent ASC and adipose spheroids in a 3D bioprinted breast cancer model

Hannes Horder¹ , David Böhringer², Nadine Endrizzi², Laura S Hildebrand¹ , Alessandro Cianciosi³ , Sabrina Stecher¹ , Franziska Dusi¹ , Sophie Schweinitzer¹, Martin Watzling¹, Jürgen Groll³ , Tomasz Jüngst³ , Jörg Teßmar³ , Petra Bauer-Kreisel¹, Ben Fabry³ and Torsten Blunk^{1,*}

¹ Department of Trauma, Hand, Plastic and Reconstructive Surgery, University Hospital Würzburg, Würzburg, Germany

² Department of Physics, University of Erlangen-Nürnberg, Erlangen, Germany

³ Chair for Functional Materials in Medicine and Dentistry at the Institute of Functional Materials and Biofabrication, University of Würzburg and Bavarian Polymer Institute, Würzburg, Germany

* Author to whom any correspondence should be addressed.

E-mail: blunk_t@ukw.de

Keywords: 3D bioprinting, adipose-derived stromal cells, adipose tissue, spheroids, migration, live-cell imaging, breast cancer model

Supplementary material for this article is available [online](#)

Abstract

Breast cancer develops in close proximity to mammary adipose tissue and interactions with the local adipose environment have been shown to drive tumor progression. The specific role, however, of this complex tumor microenvironment in cancer cell migration still needs to be elucidated. Therefore, in this study, a 3D bioprinted breast cancer model was developed that allows for a comprehensive analysis of individual tumor cell migration parameters in dependence of adjacent adipose stroma. In this co-culture model, a breast cancer compartment with MDA-MB-231 breast cancer cells embedded in collagen is surrounded by an adipose tissue compartment consisting of adipose-derived stromal cell (ASC) or adipose spheroids in a printable bioink based on thiolated hyaluronic acid. Printing parameters were optimized for adipose spheroids to ensure viability and integrity of the fragile lipid-laden cells. Preservation of the adipogenic phenotype after printing was demonstrated by quantification of lipid content, expression of adipogenic marker genes, the presence of a coherent adipo-specific extracellular matrix, and cytokine secretion. The migration of tumor cells as a function of paracrine signaling of the surrounding adipose compartment was then analyzed using live-cell imaging. The presence of ASC or adipose spheroids substantially increased key migration parameters of MDA-MB-231 cells, namely motile fraction, persistence, invasion distance, and speed. These findings shed new light on the role of adipose tissue in cancer cell migration. They highlight the potential of our 3D printed breast cancer-stroma model to elucidate mechanisms of stroma-induced cancer cell migration and to serve as a screening platform for novel anti-cancer drugs targeting cancer cell dissemination.

1. Introduction

The complex environment in which malignant tumor cells grow is decisive for processes that trigger cancer progression [1, 2]. The interplay between tumor cells and their surrounding tissue, the tumor stroma, has been shown to have distinct effects on tumor-promoting processes such as tumor cell proliferation, differentiation, and migration [3, 4]. Migration as a key feature of malignant tumor cells enables

local spreading of the primary tumor and further metastasis to distant tissues or organs, which represents a major challenge in the prognosis and therapy of aggressive cancers such as triple-negative breast cancer (TNBC) [5]. Specific parameters that define cell movement in a 3D environment, such as speed and persistence, are considered important determinants for the dissemination and metastatic capacity of the primary tumor. However, it remains to be elucidated in detail whether and how

such migration characteristics are affected by stromal cells. Conventional, widely employed assays, such as wound-healing and transwell assay, cannot properly reflect the movement of cells in the complex context of the tumor microenvironment (TME) and do not allow for a detailed analysis of such migration parameters [6, 7].

In vivo, the movement of cancer cells takes place in three-dimensional tissue and is strongly influenced by a variety of cellular, biochemical, and physical factors in this environment. The development of 3D platforms that mimic the pathophysiology of the tumor-stroma niche could enable a more in-depth analysis of specific tumor cell migration traits as a function of stromal components. This is crucial to better understand the underlying mechanisms and may help to identify specific biomarkers in this process as a basis for the development of novel drugs and therapies that target dissemination of tumor cells [8, 9].

3D bioprinting, as one of the most promising techniques in the field of biofabrication, offers the possibility to create 3D architectures with different cell types and matrix materials precisely positioned in a spatially controlled and reproducible manner [1, 10]. To date, 3D printed tumor-stroma models that demonstrate migration of cancer cells at all are rare [11, 12]. These studies have either provided endpoint imaging without quantification of migration [11], or they investigated migration in response to growth factor-laden capsules embedded in hydrogels [12]. A biofabricated 3D model that provides spatiotemporal resolution of different aspects of stroma cell-induced cancer cell migration has not been established.

In mammary tumors, adipose tissue constitutes an important part of the TME. The importance of adipose-derived stromal cells (ASCs) and adipocytes in breast cancer progression is increasingly acknowledged. Adipose and breast cancer cells are in close vicinity and interact mutually, mainly through the secretion of growth factors and cytokines, causing structural and metabolic changes of the adipose tissue. This in turn can promote, among other effects, migration and invasion of adjacent breast tumor cells, contributing to tumor cell aggressiveness [13–16]. To decipher the impact of this intricate mutual interaction on the migration behavior of tumor cells, 3D co-culture models with breast cancer cells and adipocytes or ASCs, allowing both the reciprocal crosstalk and the migration of tumor cells in a more native-like 3D environment, would be of great benefit [17]. Few studies have attempted to include adipose stroma in 3D printed breast cancer models [11, 18, 19], however, knowledge on the impact of ASCs and adipocytes on specific parameters of breast cancer cell migration is still lacking.

In a previous study, we presented a 3D adipose tissue-breast cancer model based on printed ASC spheroids that were differentiated into adipose

microtissues post-printing [19]. When co-cultured with MDA-MB-231 breast cancer cells in the printed constructs, the adipose spheroids revealed pathophysiological alterations such as reduced lipid content and profibrotic extracellular matrix (ECM) remodeling characteristic for the breast cancer niche. However, this model did not allow for examination of cancer cell migration [19].

In the present study, we developed an advanced bioprinted tumor-stroma model for the investigation of the impact of adipose microtissues on the migration of breast cancer cells in a native-like 3D environment. The set-up allowed us to analyze specific migration parameters based on live-cell imaging. ASC or pre-differentiated adipose spheroids were printed in a hyaluronic acid-based bioink in an annular shape filled with collagen I containing triple-negative MDA-MB-231 breast cancer cells. To ensure integrity and functionality after extrusion-based bioprinting, stromal spheroids were characterized regarding viability, adipose phenotype, tissue-specific ECM, and secretion behavior. The real-time analysis of tumor cell migration in the printed modular tumor-stroma model revealed that ASC and adipose spheroids distinctly increased the key migration parameters motile fraction, persistence, invasion distance, and speed of the MDA-MB-231 breast cancer cells.

2. Materials and methods

2.1. Cell culture

Human ASCs were obtained from Lonza (Basel, Switzerland; female donor, age 44, BMI 33). ASCs were cultured at 37 °C and 5% CO₂ in growth medium consisting of Dulbecco's Modified Eagle's Medium/Ham's F-12 (DMEM/F-12; Life Technologies, Carlsbad, USA) supplemented with 10% fetal bovine serum (FCS; Life Technologies), 1% penicillin/streptomycin (100 U ml⁻¹ penicillin, 0.1 mg ml⁻¹ streptomycin; Life Technologies), and 3 ng ml⁻¹ basic fibroblast growth factor (BioLegend, London, United Kingdom). Growth medium was changed every other day until cells reached 80%–85% confluency. Then, cells were passaged or harvested using 0.25% trypsin-EDTA solution (Life Technologies). For all subsequent experiments, cells at passage 6 were used.

MDA-MB-231 breast cancer cells (ATCC, Manassas, USA) were cultured in DMEM (1 g l⁻¹ glucose, Life Technologies) supplemented with 10% FCS, 1% L-glutamine, 1% MEM non-essential amino acids solution, 1% sodium pyruvate, 0.6% HEPES, and 1% penicillin/streptomycin (all Life Technologies, Carlsbad, USA) at 37 °C, 5% CO₂ until cells reached 80%–85% confluency. MDA-MB-231 is a highly aggressive, invasive and poorly differentiated TNBC cell line that lacks estrogen receptor and

progesterone receptor expression, as well as human epidermal growth factor receptor 2 amplification.

2.2. Spheroid generation and adipogenic differentiation

Spheroids were obtained utilizing agarose molds cast by MicroTissues® 3D Petri Dishes® (16 × 16 array, Sigma-Aldrich, St. Louis, USA) following the manufacturer's instructions. 640 000 ASCs/agarose mold were cultured in basal medium consisting of Preadipocyte Basal Medium-2 (Lonza, Basel, Switzerland) supplemented with 10% FCS and 1% penicillin/streptomycin for 2 d, resulting in the assembly of 256 multicellular spheroids per agarose mold (2500 cells/spheroid). Spheroids were then cultured for a further 9 d in basal medium, with media exchange every other day, and named 'ASC spheroids' in subsequent experiments. Alternatively, after the 2 d of spheroid assembly, adipogenic differentiation was induced by culture in adipogenic differentiation medium consisting of Preadipocyte Basal Medium-2 supplemented with 10% FCS, 1% penicillin/streptomycin, and insulin (final concentration 1.7 μM; PromoCell, Heidelberg, Germany), dexamethasone (1 μM; Sigma-Aldrich, St. Louis, USA), 3-isobutyl-1-methylxanthine (IBMX, 500 μM; Serva-Electrophoresis, Heidelberg, Germany) and indomethacin (200 μM; Sigma-Aldrich, St. Louis, USA) for 9 d, with media exchange every other day. These spheroids were named 'adipose spheroids' in subsequent experiments.

2.3. Preparation of hyaluronic acid-based hydrogels

Thiol-modified hyaluronic acid (HA-SH; 241 kDa) and allylated polyethylene glycol (PEG-diallyl; 6 kDa) were synthesized as previously described [20]. For hydrogel preparation, HA-SH was dissolved in HEPES buffer (154×10^{-3} M, pH = 7.6) supplemented with 4 mM CaCl₂ (Carl Roth) to reduce shear stress-induced cell damage during bioprinting [21]. Remaining hydrogel components acrylated polyethylene glycol (PEG-diacryl; Creative PEGWorks; 10 kDa), PEG-diallyl and lithium-phenyl-2,4,6-trimethylbenzoylphosphinate (LAP, Sigma-Aldrich) were dissolved in Dulbecco's Phosphate Buffered Saline (DPBS, Life Technologies) separately and mixed with HA-SH stock solution, resulting in a final hydrogel precursor solution of 0.5 wt% HA-SH, 0.25–1.50 wt% PEG-diacryl, 1.20 wt% PEG-diallyl, 0.05 wt% LAP and 2 mM CaCl₂. Concentrations of PEG-diacryl were varied to establish the optimum ratio of thiol to acryl groups for pre-crosslinking.

2.4. 3D printing and bioprinting

Printability of pre-crosslinked hydrogel formulations was assessed by manual extrusion utilizing a positive displacement pipette (Gilson, Middleton, WI) or

a BioX 3D bioprinter (Cellink, Boston, MA). G-codes for grid structure and filament fusion tests were created with HeartWare (Cellink, Boston, MA; version 2.4.1).

For 3D bioprinting, ASC or adipose spheroids (2500 cells per spheroid) were suspended in the hydrogel precursor solution (4800 spheroids/ml), transferred to 3 cc printing cartridges (Nordson EFD, Westlake, OH) and pre-crosslinked for 1 h. A DC 200 dispensing unit (Vieweg, Kranzberg, Germany) was used to evaluate bioprinting with different nozzles. Spheroid-hydrogel suspensions were extruded through a 330 or 840 μm steel nozzle (Nordson EFD, Westlake, OH; 25.4 mm length) at 40–200 kPa under sterile conditions and collected in a reaction tube. Extruded as well as cast spheroid-hydrogel suspensions were transferred into glass rings (40 μl, 5 mm diameter, 2 mm height), generating constructs of the same geometry for both printed and cast groups to enable comparability, as previously described [19]. Spheroid-laden hydrogels were crosslinked using visible light (405 nm) for 6 min. Resulting constructs were cultured for up to 24 h in serum-free co-culture medium composed of DMEM/F-12 supplemented with 1% penicillin/streptomycin. In an additional experiment, the light-induced crosslinking was omitted and the constructs (extruded as well as cast samples) were analyzed immediately after 1 h in serum-free co-culture medium.

Ring-disk model: The ring geometry for the stromal compartment was designed with Fusion 360 (Autodesk, San Rafael, CA; version 2.0.15509) and sliced with HeartWare. Hydrogel suspension with or without spheroids was printed with a BioX 3D bioprinter through an 840 μm steel nozzle at 40–55 kPa directly into 48 well-plates (Greiner Bio-One, Frickenhausen, Germany) or 3-well chamber slides (ibidi, Gräfelfing, Germany). The ring compartment consisted of two rings and was printed 5 layers in z-axis direction. Each layer was crosslinked for 1 min with the internal 405 nm LED before proceeding with the next layer. After 5 layers, the final construct was crosslinked for 5 more minutes. For the tumor compartment, MDA-MB-231 were suspended in collagen I at a concentration of 50 000 cells/ml and cast in the center of the previously printed ring compartment (100 μl/ring). The collagen I hydrogel has been previously optimized for cell migration studies and was prepared accordingly [22, 23]. Briefly, acid-dissolved rat tail collagen (Collagen R, Matrix Bioscience, Mörlenbach, Germany) was mixed with bovine skin collagen (Collagen G1, Matrix Bioscience, Mörlenbach, Germany) at a mass ratio of 1:2 and 4.5% (v/v) NaHCO₃ (23 mg ml⁻¹) and 4.5% (v/v) 10 × DMEM (Life Technologies, Carlsbad, USA) were added. 1M NaOH was used to adjust the pH of the solution to 9. Collagen was

further diluted with dilution medium (pH = 9) containing 1 volume part NaHCO_3 , 1 volume part $10 \times \text{DMEM}$ and 8 volume parts H_2O to a final concentration of 1.2 mg ml^{-1} . The hydrogel solution was polymerized at 37°C , 5% CO_2 for 1 h. The final ring-disk models were cultured in co-culture medium composed of $\text{DMEM}/\text{F-12}$ supplemented with 1% penicillin/streptomycin (i.e. without FCS) for up to 24 h. Constructs without spheroids in the ring compartment and without or with 1% or 10% FCS added to the co-culture medium served as controls. Macroscopic images of the ring-disk model were captured using an OZL-464 stereo zoom microscope (KERN, Balingen, Germany).

2.5. Rheological analysis

An Anton Paar MCR 702 rheometer (Anton Paar, Graz, Austria) with a 25 mm parallel plate geometry at a 0.5 mm gap was employed to characterize the rheological properties of different hydrogel formulations. To minimize solvent evaporation, a solvent trap was used and all experiments were performed by loading the freshly prepared hydrogel precursors on the measurement plate preheated at 37°C . Time sweep measurements were performed with 0.5% shear strain and 10 rad s^{-1} angular frequency. This oscillatory analysis was conducted to characterize the kinetics of the induced sol-to-gel transition via Michael addition for the different formulations, thus assessing the processability window of the different inks. Shear rate sweep analyses were performed from 1 to 100 s^{-1} before and after Michael addition to characterize the shear thinning behavior. The photocrosslinking of the final ink formulation (0.5 wt% HA-SH, 0.75 wt% PEG-diacryl, 1.20 wt% PEG-diallyl, and 0.05 wt% LAP) was characterized by combining a UV-vis light source (bluepoint 4, Dr Hönle AG, Gilching, Germany) equipped with a flexible light guide to the rheometer. The glass measurement plate enabled to expose the sample to UV-vis light for 60 s with a gap distance of 7.5 cm during the time sweep analysis (0.5% shear rate and 10 rad s^{-1} angular frequency). Furthermore, frequency sweeps from 100 to 1.0 rad s^{-1} were performed before and after exposure to UV-vis light.

2.6. Analysis of spheroid viability

To investigate viability of hydrogel-encapsulated spheroids, a Live/Dead Cell Staining Kit (PromoKine, Heidelberg, Germany) was used 4 h after printing. Constructs were washed in PBS before adding live/dead staining solution composed of $4 \times 10^{-6} \text{ M}$ ethidium homodimer III (EthD-III) and $1 \times 10^{-6} \text{ M}$ calcein acetoxymethyl ester (calcein-AM) in PBS. After incubation for 1 h at room temperature on an orbital shaker, images were captured using a fluorescence microscope (Olympus IX51/XC30). Stitched

fluorescent overview images of the printed ring-disk model were taken manually using the Multiple Image Alignment function of the Olympus cellSense™ Dimension Microscope Imaging Software (version 1.16) and an Olympus BX51 microscope. Fluorescent channels were stitched separately and merged with Fiji (version 1.52p) afterwards.

Cell integrity within spheroids was further assessed by quantification of lactate dehydrogenase (LDH) release using LDH-Glo™ Cytotoxicity Assay (Promega, Fitchburg, WI) according to the manufacturer's specifications. Medium supernatants were harvested 1 h after printing and transferred to LDH Storage Buffer (200 mM Tris-HCl (pH = 7.3), 10% Glycerol, 1% BSA; all obtained from Sigma-Aldrich) at a ratio of 1:20. Maximum LDH release controls of the respective conditions were generated by adding $2 \mu\text{l}$ of a 10% Triton X-100 solution (Sigma-Aldrich) per $100 \mu\text{l}$ supernatant. After 1 h of incubation, supernatants of maximum LDH release controls were harvested as described above. Results of LDH quantification were normalized to the total amount of DNA in the respective hydrogel lysates and are depicted as percentage of the total amount of LDH in the respective maximum LDH release controls.

2.7. Determination of DNA content

Spheroid-laden hydrogels were harvested and transferred to phosphate/saline buffer (50 mM phosphate buffer, 2 mM $\text{Na}_2\text{EDTA} \cdot 2\text{H}_2\text{O}$, 2 M NaCl, pH = 7.4; all obtained from Carl Roth, Karlsruhe, Germany). Subsequently, hydrogels were homogenized with a TissueLyser II (Qiagen, Hilden, Germany) at 25 Hz for 5 min, followed by sonification (Sonopuls; Bandelin electronic, Berlin, Germany). DNA content was assessed fluorometrically (Tecan GENios pro; Tecan, Crailsheim, Germany) at an excitation wavelength of 365 nm and an emission wavelength of 458 nm using Hoechst 33258 (Polysciences, Warrington, USA) and salmon sperm DNA as standard.

2.8. Quantification of intracellular lipid accumulation

Serum triglyceride determination kit (Sigma-Aldrich) was used to quantify intracellular triglyceride content of spheroids within hydrogels 24 h post-printing. After harvesting and transferring to 0.5% aqueous Thesit solution (0.5% Thesit in H_2O ; Gepepharm, Hennef, Germany), hydrogels were homogenized and sonified as described above. Lipid accumulation was determined according to the manufacturer's specifications and measured with a spectrofluorometer (Tecan GENios pro; Tecan, Crailsheim, Germany) at 570 nm. Data were normalized to the total amount of DNA in hydrogels of the respective condition.

2.9. Histological and immunohistochemical analysis

Hydrogels containing spheroids were harvested 24 h after printing and fixed in 3.7% buffered formaldehyde at 4 °C overnight. The next day, constructs were embedded in Tissue Tek O.C.T. (Sakura Finetek, Torrance, CA, USA) and incubated overnight in wet chambers at room temperature. After shock freezing in liquid nitrogen, 6 μm cryosections were prepared using a cryostat (CM 3050S, Leica, Wetzlar, Germany). For histological analysis of adipogenesis within differentiated constructs, Oil Red O was used as previously described [19]. ECM deposition and perilipin 1 expression within printed and cast spheroids were visualized immunohistochemically. Tris-EDTA buffer (10 mM Tris Base (pH = 9.0), 1 mM EDTA, 0.05% Tween 20 in H₂O; all from Sigma Aldrich) was used for antigen retrieval at 63 °C overnight. Cryosections were then carefully washed with PBS two times, followed by blocking with 1% bovine serum albumin (BSA; Sigma Aldrich) in PBS for 1 h at room temperature. Primary antibodies (anti-perilipin 1, PA5-72921, 1:100; Thermo Fisher Scientific, Waltham, MA; anti-collagen I, ab34710, 1:400; anti-collagen IV, ab19808, 1:150; anti-collagen VI, ab6588, 1:200; anti-laminin, ab11575, 1:200 and anti-fibronectin, ab2413, 1:500; all from Abcam, Cambridge, UK) diluted in 1% BSA in PBS were added and incubated at room temperature overnight in a humidified chamber. After two more washing steps with PBS, cryosections were incubated with secondary antibody (goat anti-rabbit Alexa488, ab150077, 1:400, Abcam, Cambridge, UK; diluted in 1% BSA in PBS) in a humidified chamber for 1 h at room temperature in the dark. Cryosections were washed again two times with PBS and mounted with DAPI mounting medium ImmunoSelect (Dako, Hamburg, Germany). Images were captured with a fluorescence microscope (Olympus BX51/DP71).

2.10. Protein analysis

Pierce™ BCA Protein Assay Kit (Thermo Fisher Scientific, Waltham, MA) was employed to determine total protein release of spheroid-laden hydrogels into the surrounding cell culture medium. Supernatants of cast and printed hydrogels were harvested after 1 h in culture and BCA assay was carried out following the manufacturer's instructions. Furthermore, for semi-quantitative detection of protein expression of multiple secreted cytokines and adipokines from cell culture supernatant harvested after 24 h of culture, Human Obesity Array G1 (RayBiotech, Peachtree Corners, GA) was used. DMEM/F-12 supplemented with 1% penicillin/streptomycin (serum-free co-culture medium) served as a negative control. Quantitative analysis of IL-6 and adiponectin was performed utilizing Human IL-6 and

Human Adiponectin/Acrp30 DuoSet ELISA (Bio-Techne, Minneapolis, MN), respectively. For both Human Obesity Array G1 and DuoSet ELISAs, supernatants of printed and cast hydrogel-encapsulated ASC and adipose spheroids were applied. All data were normalized to the total amount of DNA in the respective hydrogel specimens.

2.11. Quantitative reverse transcription polymerase chain reaction (qRT-PCR)

Printed and cast spheroid/hydrogel constructs were harvested after 24 h in culture, transferred into TRIzol® reagent (Thermo Fisher Scientific, Waltham, MA) and homogenized using a TissueLyser II (25 Hz, 5 min; Qiagen, Hilden, Germany). Subsequently, RNA was isolated following the manufacturer's specifications and cDNA was synthesized using the ImProm-II™ Reverse Transcription System (Promega, Mannheim, Germany). qRT-PCR was performed using a CFX96 Real-Time System (Bio-Rad, Hercules, CA) in combination with Mesa Green qPCR MasterMix Plus MeteorTaq Polymerase (Eurogentec, Seraing, Belgium) for detection. Sequences of all self-designed, intron spanning primer pairs are listed in table S1. To calculate the relative gene expression levels for each gene, the $2^{-\Delta\Delta\text{CT}}$ method [24] was applied. Gene expression of all samples was normalized to the housekeeping gene eukaryotic translation elongation factor 1 alpha (EF1 α ; self-designed) and to the gene expression of ASC spheroids without hydrogel on day 0.

2.12. Live-cell imaging

Brightfield timelapse-images of migrating breast cancer cells in the ring-disk model were acquired using a motorized microscope (Applied Scientific Instrumentation, Eugene, OR) equipped with a 4x magnification objective (Olympus, Hamburg, Germany) and a CCD camera (Lumenera Infinity 3-6UR, Ottawa, Canada) placed inside a tissue culture incubator (37 °C, 5% CO₂). Minimum intensity projected image stacks ($xyz = 2818 \times 2244 \times 300 \mu\text{m}$, voxel size = $1.024 \times 1.024 \times 10 \mu\text{m}$) were recorded every 10 min over a period of 24 h at 2–4 different fields of view per sample. Cell migration was analyzed as previously described [25, 26]. Briefly, for each time point, individual cell positions were segmented based on cross-entropy thresholding [27], and positions were connected to cell trajectories based on their Euclidean distance and temporal difference. The x/y -position of all cells was tracked in the image series based on their characteristic intensity profile in the minimal intensity projections of the z -stacks using a custom Python script [25, 28]. Only cell trajectories that were continuously tracked for at least 4 h were considered (typically ~ 450 trajectories per field of view). Cells were defined as motile if they migrated more than 10 μm within a period of 12 h [25]. For

each motile cell, the cell speed between consecutive frames was calculated and the values were averaged over the observation period for each cell trajectory and then over all cells within a field of view. In addition, the turning angles between subsequent 1 h trajectory segments per cell were calculated. Persistence values were calculated as the cosine of the turning angles and were averaged over the observation period for each cell trajectory. Consecutively, persistence values were averaged over all cell trajectories within a field of view. Further, the cell-travelled Euclidean distance (invasion distance) was calculated in subsequent 1 h trajectory segments per cell and averaged over the observation period for each cell trajectory. The 1 h invasion distance was then averaged over all cell trajectories within a field of view. Finally, velocity, persistence and the cell-travelled distance were averaged over all fields of view ($n = 8\text{--}24$) per condition.

2.13. Statistical analysis

Data are presented as mean \pm standard deviation or mean \pm standard error with at least $n = 3$ replicates per condition, if not stated otherwise. Statistical evaluation was performed using OriginPro 2021 (version 9.8.0.200) or SciPy [29] (version 1.10.1) and statistically significant differences between groups are indicated by * ($p < 0.05$). Two groups were compared by an unpaired two-sample Student's *t*-test or Welch's unequal variances *t*-test. To compare multiple groups with one independent variable, a one-way analysis of variance (ANOVA) with Bonferroni post-hoc analysis was performed. A two-way ANOVA with Bonferroni post-hoc analysis was performed to compare multiple groups with two independent variables.

3. Results

3.1. Establishment of a printable HA-SH-based ink and rheological characterization of the dual-stage crosslinking

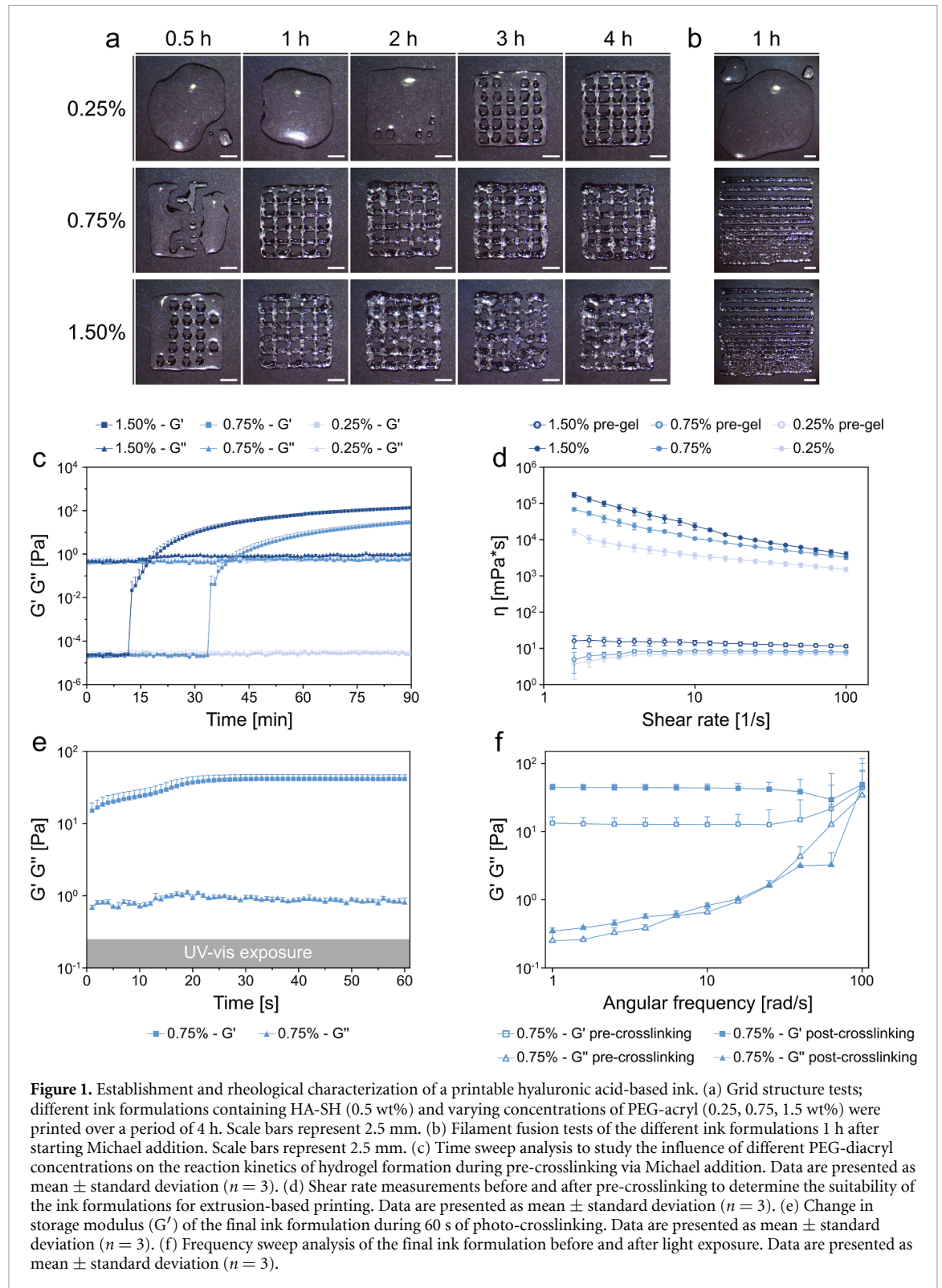
As a basis for the stromal compartment of the printed breast cancer model, a printable thiol-modified hyaluronic acid-based ink formulation was established. The ink utilized a dual-stage crosslinking mechanism, where in the first (pre-)crosslinking step thiol-modified hyaluronic acid (HA-SH) reacted with PEG-diacryl in a spontaneous Michael addition to a 3D printable, shear thinning ink. In a second step, post-printing, HA-SH was further crosslinked with PEG-diallyl in a thiol-ene reaction using the visible-light photoinitiator LAP.

Pre-crosslinking via Michael addition was investigated using 0.5 wt% HA-SH (241 kDa) and different concentrations of 10 kDa PEG-diacryl (0.25, 0.75, and 1.5 wt%). Resulting hydrogel solutions were 3D printed in different geometries or manually extruded with a positive displacement pipette and investigated over time in terms of printability and rheological

properties. Printing of grid structures over a period of 4 h allowed the different hydrogel formulations to be evaluated with regard to the time frame of printability (processing window) (figure 1(a)). 0.25 wt% PEG-diacryl led to considerably delayed Michael addition, resulting in printable grid structures not until 4 h after initiating pre-crosslinking. 1.50 wt% PEG-diacryl accelerated the Michael addition yielding complete grid structures 1 h after initiating pre-crosslinking, however, two hours later the ink started to become solid resulting in poor prints. Medium PEG-diacryl concentration (0.75 wt%) showed to be the optimal compromise between length of pre-crosslinking (1 h) and processing window (up to 4 h) (figure 1(a)). Manual extrusion experiments reflected the findings of the 3D printing evaluation: With increasing PEG-diacryl content, the Michael addition was accelerated, and medium PEG-diacryl concentrations led to a relatively long processing window (figure S1(a)). To further characterize printability, a filament fusion test was performed, where distances between ink strands consecutively decreased from 2 to 1.5, 1, 0.75 and 0.5 mm. Both inks with 1.50 and 0.75 wt% PEG-diacryl reached a resolution of at least 0.75 mm after 1 h of pre-crosslinking, with strand fusion starting at 0.5 mm (figure 1(b)).

In addition to the printing experiments, rheological characterization of the pre-crosslinking process was conducted. The initial Michael addition was examined with oscillatory analyses over time to investigate the influence of the different PEG-diacryl concentrations (0.25, 0.75, and 1.5 wt%) on the reaction kinetics of hydrogel formation. The trends of storage (G') and loss moduli (G'') showed a correlation between the PEG-diacryl concentration and the kinetics of the sol-to-gel transition. The ink formulation with the highest PEG-diacryl content (1.5 wt%) showed a crossover point ($G' = G''$) shortly after 18 min, while the precursor solution with a medium PEG-diacryl content (0.75 wt%) exhibited a sol-to-gel transition after around 40 min (figure 1(c)). The ink formulation with the lowest PEG-diacryl content (0.25 wt%) showed a much later crossover point, as revealed by extended oscillatory analysis (~ 180 min, figure S1(b)). The suitability of the ink formulations for extrusion-based 3D printing was evaluated with a shear rate sweep ($1\text{--}100\text{ s}^{-1}$) before and after Michael addition (figure 1(d)). The viscosity trends of all three ink formulations demonstrated a Newtonian behavior before initiating pre-crosslinking. After sol-to-gel transition, all inks revealed a markedly increased viscosity along with a shear-thinning behavior, which is desirable for easy extrusion through a nozzle.

After the printing process, as a second crosslinking step, a light-induced thiol-ene click reaction of the remaining thiol groups of HA-SH and the allyl moieties of 6 kDa PEG-diallyl was initiated using

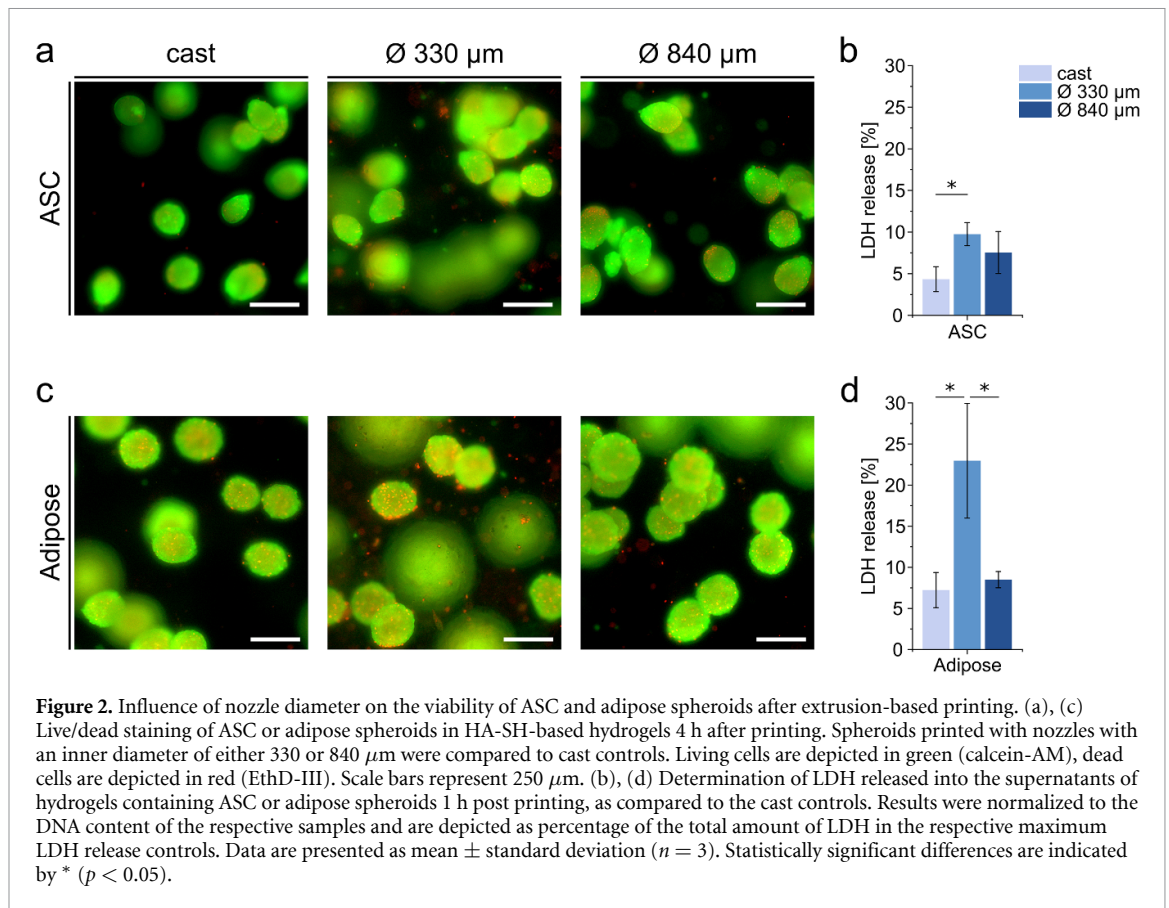


LAP. To complete the rheological assessment of the established ink, the network viscoelasticity of the final ink formulation 0.5 wt% HA-SH, 0.75 wt% PEG-diacryl, 1.2 wt% PEG-diallyl, and 0.05 wt% LAP was analyzed prior to, after, and during light-induced photo-crosslinking. During crosslinking, light exposure led to an increment of the storage modulus within the first 20 s, confirming the thiol-ene reaction (figure 1(e)). The effect of the thiol-ene reaction on

the stiffening of the ink polymer network was highlighted by a frequency sweep ($1\text{--}100\text{ rad s}^{-1}$) measurement before and after the photo-crosslinking reaction (figure 1(f)).

3.2. Influence of 3D bioprinting on viability of stromal spheroids

ASC and adipogenically differentiated (adipose) spheroids were used as 3D building blocks to print the

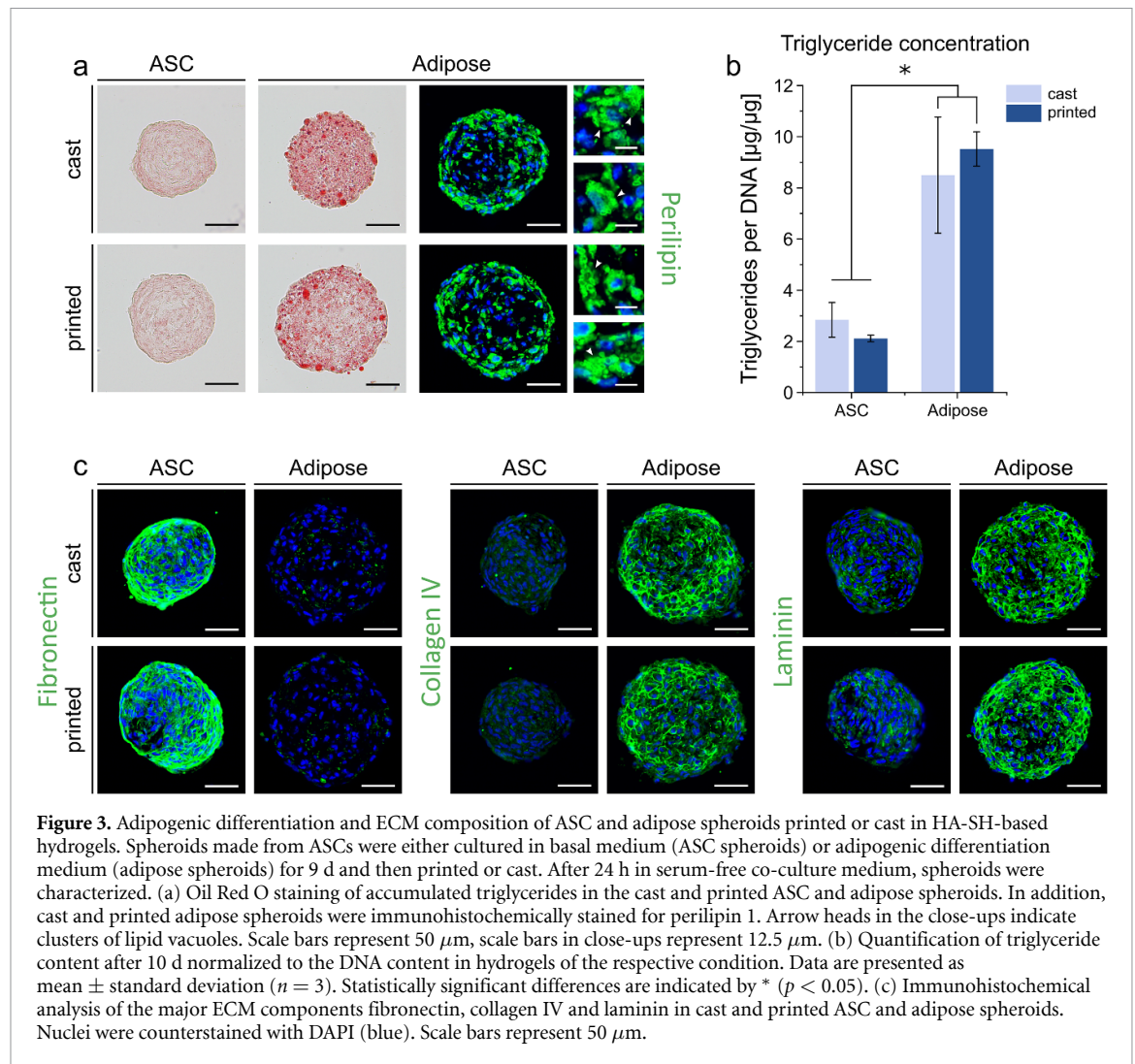


stromal part of the co-culture model. After extrusion-based bioprinting, cell viability and functionality of the spheroids were assessed. Adipose spheroids with their fragile lipid vacuoles are particularly susceptible to shear stress-induced cell damage provoked by the printing process itself. In this regard, the influence of printing nozzles with different inner diameters was examined. Applying a larger nozzle (840 μm) required less printing pressure (40–55 kPa) than a small nozzle (330 μm , 180–200 kPa). Printed and cast constructs were fabricated with an identical shape using an extrusion-based printing set-up to ensure comparability and avoid differences in nutrient and oxygen supply associated with different construct sizes and geometries [19]. ASC spheroids printed with a 330 μm nozzle exhibited a compact shape with some scattered dead cells in the surrounding hydrogel, while little to no dead cells were found in the vicinity of ASC spheroids printed with an 840 μm nozzle and in cast samples (figure 2(a)). Evaluation of LDH release as an indicator for cell damage showed a significant increase in the supernatant of ASC spheroids printed with 330 μm inner nozzle diameter as compared to the cast control (figure 2(b)). For printed adipose spheroids, the influence of the nozzle diameter on spheroid viability and cellular integrity was even more pronounced. When printed with the smaller nozzle, distinctly more dead cells were

found within or around the adipose spheroids compared to spheroids printed with the larger nozzle or in cast constructs (figure 2(c)). This observation was supported by quantification of LDH release, which was significantly higher for adipose spheroids printed with the 330 μm nozzle ($22.97 \pm 6.98\%$ of total LDH release) than for spheroids printed with the 840 μm nozzle ($8.50 \pm 0.98\%$ of total LDH release) or cast samples ($7.23 \pm 2.14\%$ of total LDH release) (figure 2(d)). Additionally, the quantification of total protein in the supernatants of constructs printed with the 840 μm nozzle and cast constructs showed no distinct differences indicating that proteins were not being released in an uncontrolled manner by damaged cells (figure S2). Taken together, conditions were established enabling the printing of ASC and, in particular, adipogenically differentiated spheroids without compromising their viability. Based on these findings, the 840 μm nozzle was used for all subsequent bioprinting experiments.

3.3. Adipogenic phenotype and secretion behavior of printed stromal spheroids

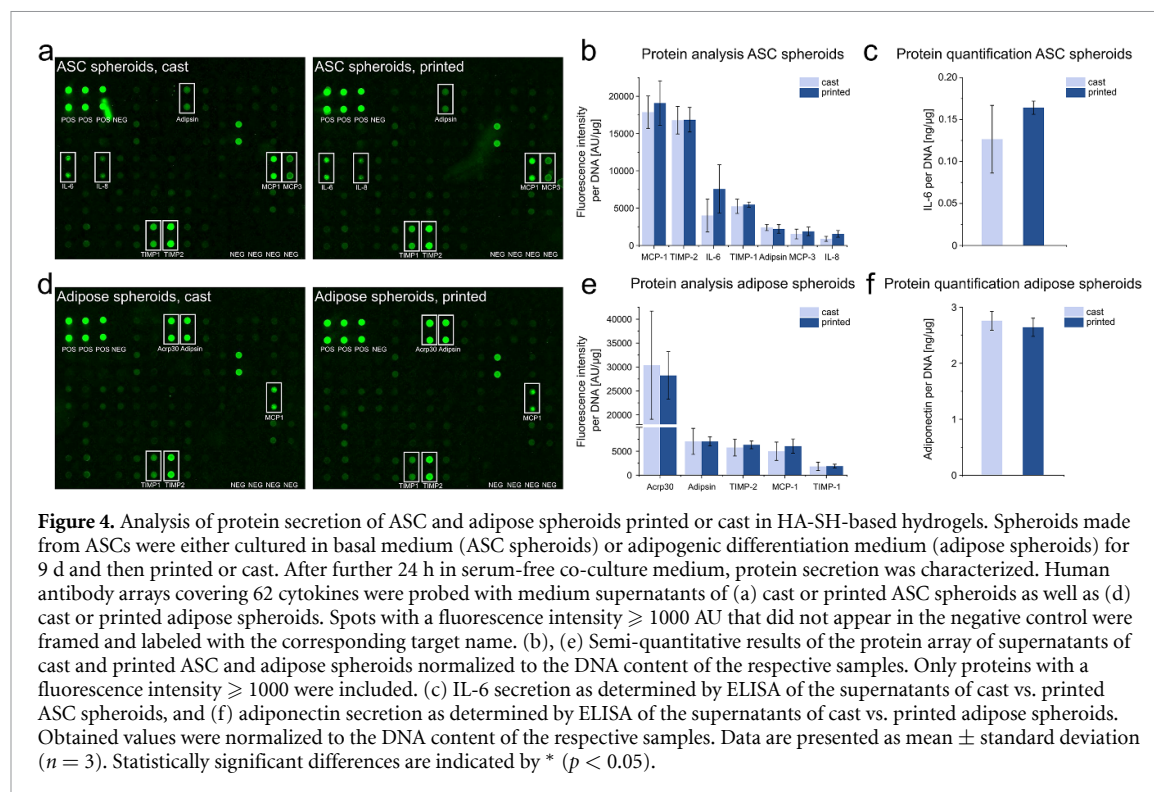
Printed adipogenically differentiated spheroids were further characterized regarding their adipose phenotype and compared to cast spheroids to exclude any adverse effects of the printing process. The same comparison was applied to printed and cast



non-differentiated ASC spheroids. A distinct staining with Oil Red O for accumulated lipids was observed in both cast and printed adipose constructs indicating considerable adipogenic differentiation, whereas no lipid droplets were apparent in constructs with ASC spheroids (figure 3(a)). Fat vacuoles were intact and exhibited a stable round morphology after printing as demonstrated by perilipin 1 immunohistochemical staining (figure 3(a), close-up view). Quantitative determination of intracellular triglyceride levels confirmed marked adipogenesis in adipogenically induced spheroids with significantly higher triglyceride content compared to their non-induced counterparts (figure 3(b)). Triglyceride levels were similar in cast and printed adipose spheroids. These findings were further supported by gene expression analysis of the adipogenic marker genes $PPAR\gamma$ as a key transcription factor of adipogenic differentiation, and fatty acid-binding protein 4 (FABP4) as a late marker of adipogenesis (figure S3(a)). Expression levels of both markers were similarly elevated in cast and printed adipose samples compared to the respective ASC spheroids.

Besides lipid accumulation, adipogenesis involves the development of a characteristic ECM profile [30]. To ensure that the extrusion-based printing process did not alter ECM composition of ASC and adipose spheroids, major ECM components of cast and printed spheroids were immunohistochemically analyzed (figure 3(c)). ASC spheroids revealed a distinct expression of fibronectin, while the main components of the basement membrane of adipocytes, collagen IV and laminin, were hardly detectable. Adipose spheroids, on the contrary, displayed high expression levels of collagen IV and laminin but very low fibronectin expression. Staining intensity was comparable in cast and printed constructs, which was also confirmed by additional staining for collagen I and VI (figure S3(b)).

Whereas all experiments described so far were done with cast or printed spheroids after the final light-induced thiol-ene crosslinking, an additional experiment was performed with adipose spheroids immediately after casting or printing, i.e. without the light-induced crosslinking step. The results of the LDH release, live/dead and lipid droplet staining,



and staining of ECM components again showed no differences between cast and printed samples, confirming that there were no adverse effects of the printing process (figure S4). Additionally, by comparing results of figure S4 (without light-induced crosslinking) with figures 2 and 3 (after crosslinking), also no detrimental effects of the stiffening of the ink polymer network which was caused by the light-induced crosslinking (see figure 1(f)) could be detected.

In the developed adipose stroma-breast cancer model, ASC and adipose spheroids printed in the ring compartment can interact with the cancer cells located in the disk compartment through secreted molecules such as cytokines, chemokines and adipokines. Therefore, it was crucial to ensure that this mode of interaction would still be functional after the complete printing process. To this end, supernatants of printed and cast ASC and adipose spheroids were analyzed for a broad range of cytokines utilizing a protein array (figures 4(a) and (d)). The following proteins with prominent expression were discovered in the supernatants of ASC spheroid-laden hydrogels: Monocyte chemotactic protein 1 (MCP1/CCL-2), tissue inhibitor of metalloproteinases 2 (TIMP-2), interleukin 6 (IL-6), tissue inhibitor of metalloproteinases 1 (TIMP-1), adipin, monocyte chemotactic protein 3 (MCP-3/CCL-7), and interleukin 8 (IL-8) (figure 4(b)). Cast and printed constructs exhibited no significant difference in expression levels of these proteins. In addition, the cancer-related cytokine IL-6 was quantitatively

determined via ELISA (figure 4(c)). No distinct difference in protein secretion per DNA between the two conditions (cast/printed) could be detected (cast: 0.13 ± 0.04 ng μg^{-1} , printed: 0.16 ± 0.01 ng μg^{-1}). In the supernatants of printed adipose spheroids, adiponectin (Acrp30), adipin, TIMP-2, MCP-1, and TIMP-1 were prominent (figure 4(e)), again with similar expression levels for cast and printed samples. Quantitative analysis of adiponectin also revealed no significant differences between cast and printed samples (cast: 2.76 ± 0.17 ng μg^{-1} , printed: 2.64 ± 0.16 ng μg^{-1}) (figure 4(f)). Taken together, extrusion-based bioprinting of stromal spheroids in a hyaluronic acid-based ink had no adverse effect on the adipogenic phenotype of differentiated spheroids, deposited ECM, and cytokine secretion.

3.4. Ring-disk co-culture model set-up to investigate breast cancer cell migration

After ensuring the integrity and functionality of the spheroids in the printed stromal compartment, the breast cancer co-culture model was developed. The model was specifically designed to study 3D migration of tumor cells depending on the paracrine stimulation of adjacent stromal cells utilizing live-cell imaging. Therefore, tumor and stromal cells were spatially separated resulting in a modular design with a bioprinted outer ring compartment composed of HA-SH-based ink with stromal cell spheroids and an inner disk compartment consisting of MDA-MB-231 cells in collagen I (figure 5(a)). This modular set-up allowed us to study the effects of ASC and

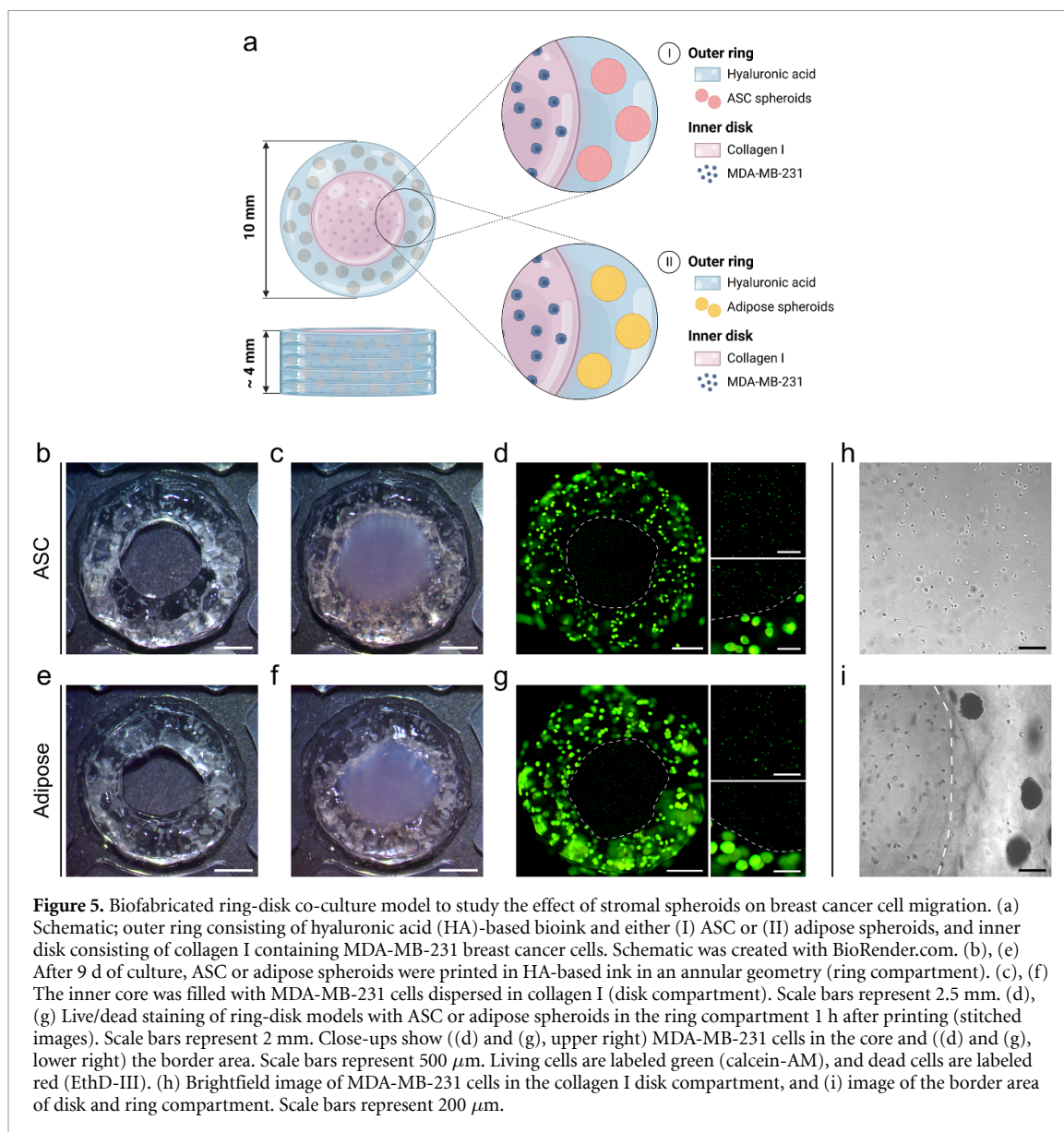


Figure 5. Biofabricated ring-disk co-culture model to study the effect of stromal spheroids on breast cancer cell migration. (a) Schematic; outer ring consisting of hyaluronic acid (HA)-based bioink and either (I) ASC or (II) adipose spheroids, and inner disk consisting of collagen I containing MDA-MB-231 breast cancer cells. Schematic was created with BioRender.com. (b), (e) After 9 d of culture, ASC or adipose spheroids were printed in HA-based ink in an annular geometry (ring compartment). (c), (f) The inner core was filled with MDA-MB-231 cells dispersed in collagen I (disk compartment). Scale bars represent 2.5 mm. (d), (g) Live/dead staining of ring-disk models with ASC or adipose spheroids in the ring compartment 1 h after printing (stitched images). Scale bars represent 2 mm. Close-ups show ((d) and (g), upper right) MDA-MB-231 cells in the core and ((d) and (g), lower right) the border area. Scale bars represent 500 μm . Living cells are labeled green (calcein-AM), and dead cells are labeled red (EthD-III). (h) Brightfield image of MDA-MB-231 cells in the collagen I disk compartment, and (i) image of the border area of disk and ring compartment. Scale bars represent 200 μm .

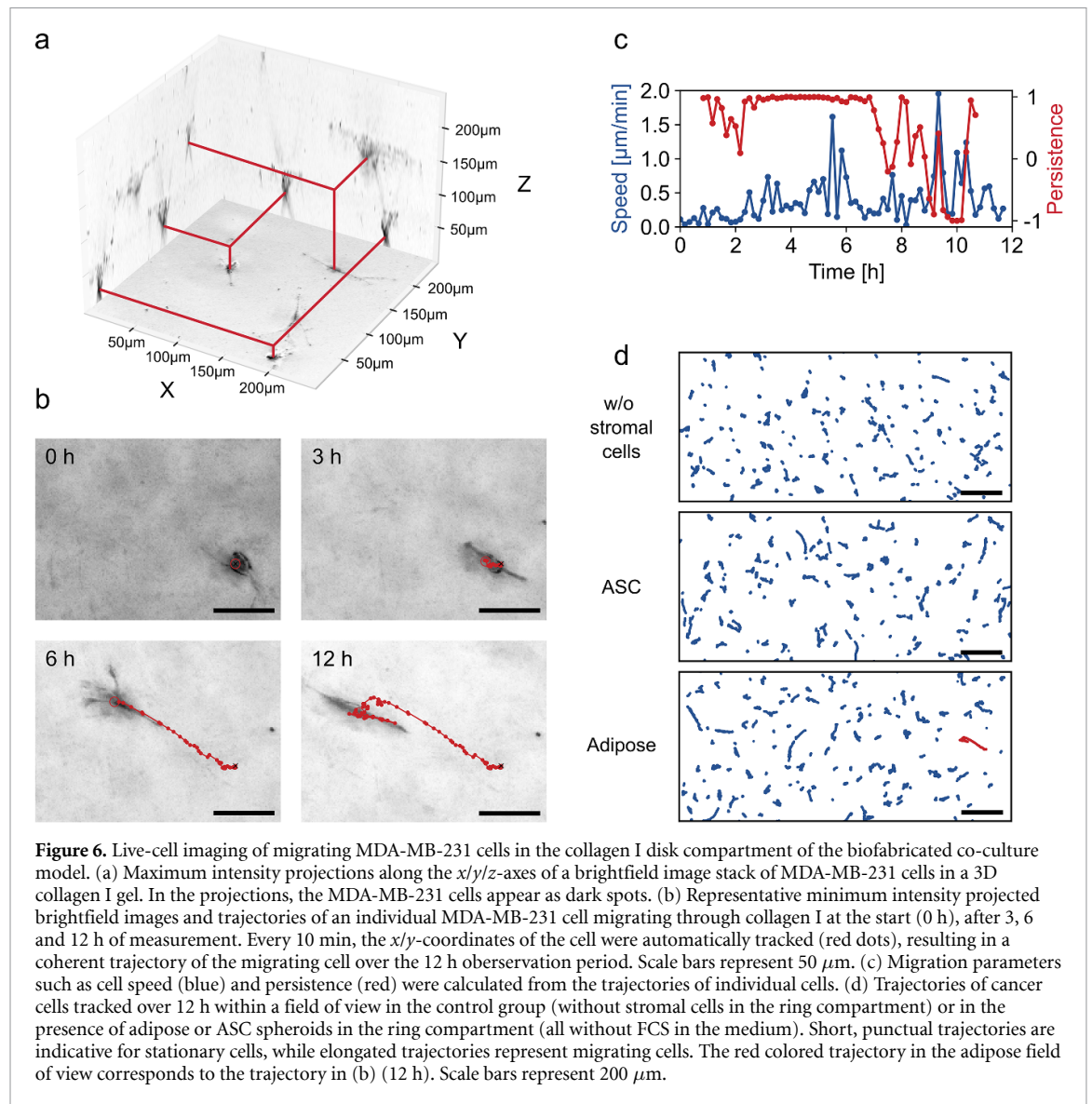
adipose spheroids on cancer cell migration individually (figure 5(a-I, II)). ASC or adipose spheroids were suspended in HA-SH-based ink after 9 d of culture, and were bioprinted in a ring geometry (10 mm outer diameter) (figures 5(b) and (e)). The printed annular geometry consisted of 2 rings printed in close proximity to form a coherent ring structure (figure S5). The resulting inner core was filled with MDA-MB-231 cells suspended in collagen I, completing the ring-disk model (figures 5(c) and (f)). Representative brightfield images of MDA-MB-231 cells in the collagen I disk are shown in figures 5(h) and (i). Live/dead staining immediately after printing revealed good viability of ASC and adipose spheroids as well as MDA-MB-231 cells (figures 5(d) and (g)).

3.5. Analysis of stromal cell-induced stimulation of MDA-MB-231 cell migration

To investigate breast cancer cell migration under the influence of the adipose stromal compartment,

the movement of single MDA-MB-231 cells in the tumor compartment was recorded using a custom-made live-cell imaging set-up. Image-based migration analysis is exemplified in figure 6. Cell trajectories were tracked automatically based on intensity projected brightfield images recorded every 10 min over a period of 24 h [25, 26]. Maximum intensity projections along the $x/y/z$ -axes of a brightfield image stack of MDA-MB-231 cells are shown in figure 6(a). The trajectory of a single MDA-MB-231 cell after 3, 6 and 12 h is depicted in figure 6(b) for illustration. Each data point (red dot) corresponds to the x/y -position of the cell measured every 10 min.

Based on the resulting cell trajectory, characteristic migration parameters such as migration speed and persistence (figure 6(c)), as well as invasion distance, were computed. Migration speed was computed from the average Euclidean distance between x/y -positions of the same cell in consecutive frames. Persistence as a measure for directionality of cell

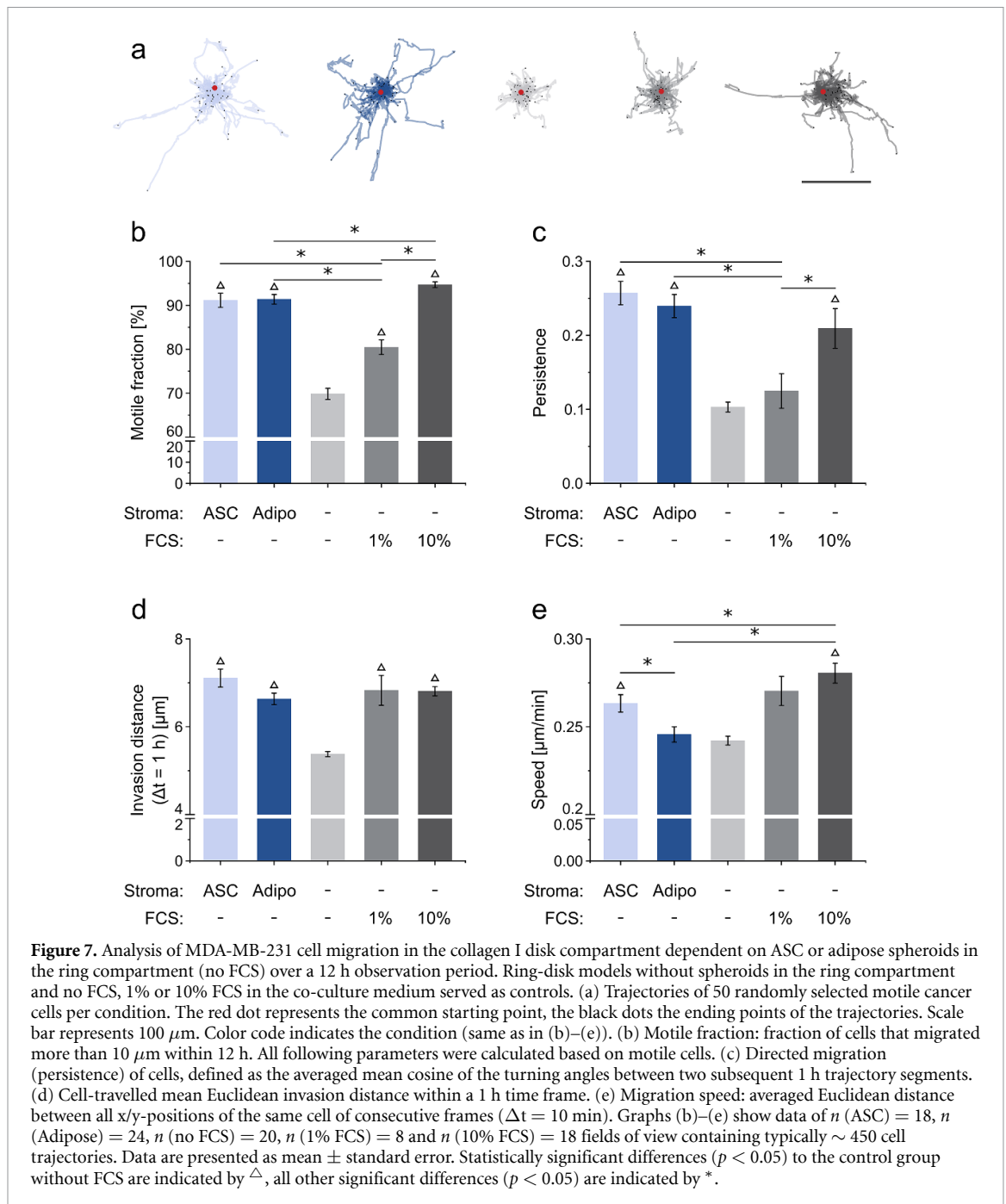


migration was defined as the average mean cosine of the turning angles between two consecutive 1 h trajectory segments. Invasion distance corresponded to the mean Euclidean distance a cell migrated within a 1 h time frame. Figure 6(d) shows the trajectories of MDA-MB-231 cells of one field of view after 12 h in the presence of ASC or adipose spheroids compared to control (no spheroids in the ring compartment, no FCS in the co-culture medium). While trajectories of MDA-MB-231 breast cancer cells in the control condition were mostly short, the trajectories of many cancer cells were longer and straighter in the presence of ASC or adipose spheroids.

The effect of ASC and adipose spheroids in the stromal ring on the migration behavior of MDA-MB-231 cells was quantified by the migration parameters mentioned above and compared to a cell-free stromal compartment (all without FCS in the medium). Serum was omitted to avoid effects of exogenous cytokines and growth factors from FCS, and

to clearly reveal the effects of secreted factors of the ASCs or adipocytes in the stromal compartment on the migration behavior of the breast cancer cells. 1% and 10% FCS in the medium served as further controls. For computing the average speed, invasion distance, and persistence, only the motile fraction of MDA-MB-231 cells was included in the analysis, i.e. cells that migrated more than 10 μm within a 12 h observation period.

After 12 h, most MDA-MB-231 cells in the presence of ASC or adipose spheroids were classified as motile ($91.14 \pm 1.60\%$ and $91.38 \pm 1.10\%$, respectively), while the fraction of motile tumor cells was distinctly lower in the absence of stromal ASC or adipose spheroids ($69.85 \pm 1.27\%$). The migration-promoting effect of stromal spheroids on the motile fraction was comparable to that of 10% FCS in the medium ($94.70 \pm 0.66\%$) (figure 7(b)). Analysis of directional persistence revealed a similar effect. Persistence in the movement of the tumor cells was



significantly increased in the presence of ASC and adipose spheroids in the ring compartment as compared to the spheroid-free negative control (without FCS) (figure 7(c)). Again, the impact of the stromal spheroids was comparable to that of 10% FCS in the positive control group. With regard to invasion distance, MDA-MB-231 cells migrated $7.11 \pm 0.20 \mu\text{m}$ and $6.63 \pm 0.13 \mu\text{m}$ on average within a 1 h time frame when exposed to ASC and adipose spheroids, respectively (figure 7(d)). The average distance covered by MDA-MB-231 cells without spheroids in the stromal compartment (without FCS) was distinctly lower ($5.38 \pm 0.06 \mu\text{m}$). This effect was additionally illustrated by depicting the cell tracks

of 50 randomly picked motile MDA-MB-231 cells over the 12 h observation period for each condition (figure 7(a)). When ASC (light blue) or adipose spheroids (dark blue) were present in the ring compartment, cell trajectories were considerably longer, as compared to the spheroid-free (without FCS) control (light grey). Migration speed was promoted only by ASC spheroids, whereas adipose spheroids had no distinct effect on this parameter compared to the cell-free ring condition after 12 h (figure 7(e)). Additionally to the 12 h period, in figure S6 the migration behavior after 6 and 24 h is shown, with similar results. After 24 h, also the migration speed was increased by both types of stromal spheroids,

as compared to the cell-free ring (figure S6). As an additional measure, the directed migration towards the outer stromal compartment was assessed. A slight trend was observed that in the presence of ASC and adipose spheroids, the cancer cells preferentially migrated towards the outer ring, while this was not the case for control conditions without spheroids in the outer ring; however, this effect was not statistically significant (figure S7). Taken together, stromal ASC and adipose spheroids clearly increased specific migration parameters in TNBC cells such as the fraction of motile cells, persistence, speed, and invasion distance.

4. Discussion

Adipocytes and ASCs are key components of the mammary stroma and as such play essential roles in the breast cancer microenvironment supporting cancer progression [13, 16]. In this context, the specific role of these neighboring cells in cancer cell migration, which represents a key feature in cancer progression, is still poorly understood. To accurately recapitulate this complex interaction in the TME, biofabrication technologies such as bioprinting or microfluidic approaches provide the means to achieve defined spatial arrangements of cells or matrix [10, 31–34]. Yet, advanced models for the detailed investigation of tumor cell migration traits as a function of stromal cells are still lacking. Therefore, in this study, we developed a biofabricated 3D co-culture model for live-cell imaging analysis of breast cancer cell migration parameters in dependence of adjacent stromal cells from adipose tissue.

Different strategies have been applied for the biofabrication of 3D adipose tissue mainly using ASCs printed as single cells in different hydrogel systems followed by adipogenic differentiation post-printing [35, 36]. Few studies have also printed pre-differentiated adipocytes or isolated mature adipocytes [37, 38]. These studies mainly aimed to engineer 3D adipose constructs in the context of regenerative medicine. Here, we bioprinted an adipose compartment to be integrated in our breast cancer-stroma model. The printed model exhibits a ring-disk geometry with a central tumor region surrounded by a ring of adipose stroma and thus mimics the architecture of the early breast cancer microenvironment. For this purpose, we chose to print adipose spheroids since direct printing of 3D cellular aggregates allows controlled spatial arrangement in complex hierarchical structures that can be used immediately to investigate a native tissue-like functional response.

For spheroid printing, a hyaluronic acid-based, dual-stage crosslinked bioink formulation was established in this study. Hyaluronic acid is part of the

ECM of adipose tissue [39, 40] and also a component of the breast cancer TME and as such constitutes a suitable matrix for the adipose compartment of the co-culture model. In the first step of the dual-stage crosslinking mechanism, the processing window provided sufficient time for bioprinting of the stromal compartment in a high-throughput manner, while the short pre-crosslinking time was favorable to prevent sedimentation of spheroids during and after the printing process and thus uneven distribution within the printed constructs. This is crucial when printing spheroids, as these cell aggregates are heavier than single cells and therefore tend to sediment quickly in low-viscosity fluids. Shear rate measurements of the pre-crosslinked gel revealed an adequate viscosity that was distinctly higher than that of a different hyaluronic acid-based gel system used for spheroid printing in a previous study, so that no additional thickener was required [19]. Rheological characterization demonstrated shear-thinning behavior of the pre-crosslinked gel, which is known to increase survival of cells due to reduced shear stress when applied for extrusion-based printing [41]. Previously, a similar HA-based hydrogel has been utilized for the chondrogenic differentiation of mesenchymal stromal cells [20], however, has not been adapted for spheroid printing. Furthermore, in the current study, LAP was used as photoinitiator instead of I2959 [20] enabling efficient visible light (405 nm) polymerization during the second crosslinking stage, which is also beneficial for cell viability and metabolic activity compared to the use of I2959 in UV-polymerized gels [42, 43].

As adipocytes are highly fragile cells due to their lipid-filled vacuoles, the printing parameters had to be carefully adjusted to ensure viability and integrity of the printed adipose microtissues. During extrusion-based printing, shear stress within the nozzle is widely regarded as the leading cause of cell impairment [44–47] and can be minimized by adjusting pressure and nozzle inner diameter accordingly [48]. Here, we found that the use of a larger nozzle resulted in lower printing pressure and yielded constructs with highly viable adipose spheroids. So far, printing of adipose spheroids has hardly been realized. Colle *et al* recently have shown bioprinting of albeit smaller adipogenically differentiated spheroids in GelMA as proof-of-principle, however, an in-depth functional and structural assessment of the adipose phenotype after printing has not been conducted [49]. In the present study, a comprehensive characterization of the printed adipose microtissues indicated that the adipogenic phenotype in terms of intact lipid vacuoles, lipid content, and expression of adipogenic marker genes was not affected by the printing process. Furthermore, adipose spheroids acquired a tissue-specific extracellular matrix, which was also retained after printing, with high laminin and collagen IV expression and a very low fibronectin

expression, as described previously for adipose spheroids differentiated for 9 d [19, 30]. Direct printing of pre-differentiated adipose spheroids enabled the design of an unbiased co-culture system where migration analysis of breast cancer cells was not affected by serum or differentiation cocktail residues in the HA-based ink.

In the TME, adipocytes and ASCs interact with neighboring breast cancer cells mostly via paracrine crosstalk [16, 50]. In the printed adipose compartment, both ASC and adipose spheroids exhibited a secretion pattern with various cytokines and matrix-remodeling factors. An adipose-specific profile was shown for the adipogenically differentiated spheroids with the expression of adipokines such as adiponectin and adipisin [51, 52]. Secretion apparently was not affected by the printing process as the pattern and concentration of secreted proteins in the cast und printed constructs were comparable.

To date, very few printed 3D adipose-breast cancer models have been realized mostly representing proof-of-principle studies. Chaji *et al* have printed mixed pre-differentiated ASCs and tumor cells in alginate/gelatin ink [18]. Vinson *et al* have incorporated cancer cell-laden microbeads into bulk hydrogel containing differentiated adipocytes by laser direct-write printing [11]. In both studies, the primary focus was on the development of the bioink, printing process and co-culture conditions; a comprehensive analysis of the adipose phenotype or tumor cell migration has not been performed.

In general, detailed knowledge is still lacking on how adipose stromal cells such as ASCs and adipocytes affect specific migration properties of breast cancer cells such as cell speed and persistence, parameters that essentially determine the efficiency of migration and are closely linked with cancer invasion and dissemination [53, 54]. To the best of our knowledge, this study is the first presentation of a 3D printed breast cancer model that allows a comprehensive analysis of individual tumor cell migration parameters in dependence of adjacent adipose stroma.

Tumor cell migration has typically been visualized and analyzed in 2D systems. Current research is now seeking to integrate the complex structural organization of the TME in 3D models using printing technologies. However, in the context of breast cancer, such models are still lacking real-time resolution of the dynamic migration process [11, 55–57] depending on neighboring stromal cells, which is a major feature of our newly developed model.

Tracking the motion of individual MDA-MB-231 breast cancer cells clearly revealed marked effects of ASCs and adipocytes on key migration parameters in a 3D environment. Compared to the control group (no spheroids in the stromal ring compartment), the fraction of motile tumor cells was markedly elevated to more than 90% migrating cells in the presence of

ASC or adipose spheroids. Motile cells covered significantly larger distances and migrated faster and in a more persistent manner under the influence of either ASCs or adipocytes. Furthermore, a trend of directed migration towards the adipose compartments was observed.

ASC and adipose spheroids exerted a similar effect on the motile fraction, persistence, invasion distance, and migration speed while partly different secretion patterns of the two cell types were apparent in protein analysis. Cytokines such as IL-6 and MCP-1, which were present in the secretome of the printed adipose compartments, have been reported to generally promote breast cancer cell migration [58, 59]. However, whether and how these factors influence specific migration parameters is not known.

In this context, a recent study investigating the effect of macrophages on the migration behavior of breast cancer cells has shown that specific migration characteristics such as speed and persistence can be individually modulated through different mechanisms. Macrophages increased cancer cell migration speed mainly through TGF- β 1-induced MT1-MMP expression in cancer cells, whereas macrophage-released TNF α and TGF- β 1 synergistically enhanced cancer cell migration persistence via NF- κ B-dependent MMP1 expression in a 3D environment [60]. This emphasizes the relevance of characterizing how a certain stimulus affects different aspects of cancer cell migration (e.g. speed and persistence) in 3D ECM to gain a detailed and quantitative understanding of tumor dissemination. The availability of advanced 3D co-culture models, such as the adipose-breast cancer model presented here, will help to get a deeper insight into the complex interactions in the adipose TME that govern breast cancer cell migration. For example, the model can be used in further studies to investigate the influence of specific adipose tissue factors on the individual migration characteristics of tumor cells, also as a function of extrinsic parameters such as matrix stiffness or fiber orientation.

In follow-up studies, the stromal compartment can be modified to integrate different stages of adipose tissue development. Although spheroids developed into adipose microtissues, the 9 d differentiation might have underestimated the differences between the ASC and adipose spheroid group. Variation of the feeding regime and prolonged differentiation times may result in even more mature adipose microtissues, including modulation of the secretion profile and the triglyceride content. As a further comparison to the ASC spheroids applied here, also undifferentiated and differentiated ASCs as single cells may be included. Moreover, in the current study, the HA-based bioink for the ring compartment was chosen to prevent cancer cell migration into this compartment. Further ink developments may be

integrated in the model that also allow migration into the neighboring compartment. This may provide more detailed insight into the mechanisms that promote the directional migration and dissemination of breast cancer cells into the surrounding adipose tissue. The promotion of migration dynamics by ASCs should also be taken into account when investigating these cells in the context of cell-assisted lipotransfer for breast reconstruction after mastectomy with regard to the oncological safety of this procedure [16].

In conclusion, in this study, we developed a 3D bioprinted co-culture model that enables a comprehensive analysis of individual tumor cell migration parameters in dependence of adjacent adipose stroma. A hyaluronic acid-based ink was established that is suitable for printing ASC and adipose spheroids while maintaining viability, integrity, adipose phenotype and secretion behavior, which are hallmarks of functional adipose tissue. Live-cell imaging within the model revealed that both ASC and adipose spheroids markedly increased key parameters of the migration process, namely the motile fraction, migration persistence, invasion distance, and speed of MDA-MB-231 breast cancer cells, thus markedly enhancing the overall invasion efficiency of the tumor cells. Our results provide new insights into how adipose tissue promotes the dissemination of breast cancer cells. We propose that our model has the potential for further in-depth analysis of key aspects of stroma-mediated migration of tumor cells and to serve as a screening platform for novel anti-cancer drugs targeting cancer cell migration.

Data availability statement

The data cannot be made publicly available upon publication because they are not available in a format that is sufficiently accessible or reusable by other researchers. The data that support the findings of this study are available upon reasonable request from the authors.

Acknowledgments

The authors thank Annett Hoffmann and Mohammed Hankir, University Hospital Würzburg, Germany, for excellent technical assistance with histology.

This work was funded by the Deutsche Forschungsgemeinschaft (DFG, German Research Foundation), Project Number 326998133, TRR 225 (subprojects C02, A01, A02, B09).

ORCID iDs


Hannes Horder  <https://orcid.org/0009-0006-9699-6712>

Laura S Hildebrand  <https://orcid.org/0000-0002-1522-9591>

Alessandro Cianciosi  <https://orcid.org/0009-0009-1314-4437>

Sabrina Stecher  <https://orcid.org/0000-0001-5336-7058>

Franziska Dusi  <https://orcid.org/0009-0006-0131-7490>

Jürgen Groll  <https://orcid.org/0000-0003-3167-8466>

Tomasz Jüngst  <https://orcid.org/0000-0002-2458-8713>

Jörg Teßmar  <https://orcid.org/0000-0001-7057-5369>

Torsten Blunk  <https://orcid.org/0000-0003-1050-6753>

References

- [1] Rodrigues J, Heinrich M A, Teixeira L M and Prakash J 2021 3D *in vitro* model (R)evolution: unveiling tumor-stroma interactions *Trends Cancer* **7** 249–64
- [2] Anderson N M and Simon M C 2020 The tumor microenvironment *Curr. Biol.* **30** R921–R5
- [3] Ungefroren H, Sebens S, Seidl D, Lehnert H and Hass R 2011 Interaction of tumor cells with the microenvironment *Cell Commun. Signal.* **9** 18
- [4] Fares J, Fares M Y, Khachfe H H, Salhab H A and Fares Y 2020 Molecular principles of metastasis: a hallmark of cancer revisited *Signal Transduct. Target. Ther.* **5** 28
- [5] Neophytou C, Boutsikos P and Papageorgis P 2018 Molecular mechanisms and emerging therapeutic targets of triple-negative breast cancer metastasis *Front. Oncol.* **8** 31
- [6] Solbu A A, Caballero D, Damigos S, Kundu S C, Reis R L, Halaas O, Chahal A S and Strand B L 2023 Assessing cell migration in hydrogels: an overview of relevant materials and methods *Mater. Today Bio* **18** 100537
- [7] Katt M E, Placone A L, Wong A D, Xu Z S and Seanson P C 2016 *In vitro* tumor models: advantages, disadvantages, variables, and selecting the right platform *Front. Bioeng. Biotechnol.* **4** 12
- [8] Roarty K and Echeverria G V 2021 Laboratory models for investigating breast cancer therapy resistance and metastasis *Front. Oncol.* **11** 645698
- [9] Augustine R, Kalva S N, Ahmad R, Zahid A A, Hasan S, Nayeem A, McClements L and Hasan A 2021 3D bioprinted cancer models: revolutionizing personalized cancer therapy *Transl. Oncol.* **14** 101015
- [10] Shukla P, Yeleswarapu S, Heinrich M A, Prakash J and Pati F 2022 Mimicking tumor microenvironment by 3D bioprinting: 3D cancer modeling *Biofabrication* **14** 032002
- [11] Vinson B T *et al* 2017 Laser direct-write based fabrication of a spatially-defined, biomimetic construct as a potential model for breast cancer cell invasion into adipose tissue *Biofabrication* **9** 025013
- [12] Meng F, Meyer C M, Joung D, Vallera D A, McAlpine M C and Panoskaltis-Mortari A 2019 3D bioprinted *in vitro* metastatic models via reconstruction of tumor microenvironments *Adv. Mater.* **31** e1806899
- [13] Wu Y, Li X, Li Q, Cheng C and Zheng L 2022 Adipose tissue-to-breast cancer crosstalk: comprehensive insights *Biochim. Biophys. Acta* **1877** 188800
- [14] Choi J, Cha Y J and Koo J S 2018 Adipocyte biology in breast cancer: from silent bystander to active facilitator *Prog. Lipid Res.* **69** 11–20
- [15] Sabol R A, Giacomelli P, Beighley A and Bunnell B A 2019 Adipose stem cells and cancer: concise review *Stem Cells* **37** 1261–6
- [16] Brock C K *et al* 2021 A role for adipocytes and adipose stem cells in the breast tumor microenvironment and regenerative medicine *Front. Physiol.* **12** 751239

- [17] Frohlich E 2023 The variety of 3D breast cancer models for the study of tumor physiology and drug screening *Int. J. Mol. Sci.* **24** 7116
- [18] Chaji S, Al-Saleh J and Gomillion C T 2020 Bioprinted three-dimensional cell-laden hydrogels to evaluate adipocyte-breast cancer cell interactions *Gels* **6** 10
- [19] Horder H et al 2021 Bioprinting and differentiation of adipose-derived stromal cell spheroids for a 3D breast cancer-adipose tissue model *Cells* **10** 803
- [20] Hauptstein J, Forster L, Nadernezhad A, Horder H, Stahlhut P, Groll J, Blunk T and Tessmar J 2022 Bioink platform utilizing dual-stage crosslinking of hyaluronic acid tailored for chondrogenic differentiation of mesenchymal stromal cells *Macromol. Biosci.* **22** e2100331
- [21] Fischer L et al 2022 Calcium supplementation of bioinks reduces shear stress-induced cell damage during bioprinting *Biofabrication* **14** 045005
- [22] Steinwachs J, Metzner C, Skodzek K, Lang N, Thievensen I, Mark C, Munster S, Aifantis K E and Fabry B 2016 Three-dimensional force microscopy of cells in biopolymer networks *Nat. Methods* **13** 171–6
- [23] Lang N R, Skodzek K, Hurst S, Mainka A, Steinwachs J, Schneider J, Aifantis K E and Fabry B 2015 Biphasic response of cell invasion to matrix stiffness in three-dimensional biopolymer networks *Acta Biomater.* **13** 61–67
- [24] Livak K J and Schmittgen T D 2001 Analysis of relative gene expression data using real-time quantitative PCR and the 2⁻(delta delta C(T)) method *Methods* **25** 402–8
- [25] Condor M, Mark C, Gerum R C, Grummel N C, Bauer A, Garcia-Aznar J M and Fabry B 2019 Breast cancer cells adapt contractile forces to overcome steric hindrance *Biophys. J.* **116** 1305–12
- [26] Hazur J, Endrizzi N, Schubert D W, Boccaccini A R and Fabry B 2022 Stress relaxation amplitude of hydrogels determines migration, proliferation, and morphology of cells in 3-D culture *Biomater. Sci.* **10** 270–80
- [27] Li C H and Lee C K 1993 Minimum cross entropy thresholding *Pattern Recogn.* **26** 617–25
- [28] Metzner C, Mark C, Steinwachs J, Lautscham L, Stadler F and Fabry B 2015 Superstatistical analysis and modelling of heterogeneous random walks *Nat. Commun.* **6** 7516
- [29] Virtanen P et al 2020 SciPy 1.0: fundamental algorithms for scientific computing in Python *Nat. Methods* **17** 261–72
- [30] Hoefner C et al 2020 Human adipose-derived mesenchymal stromal/stem cell spheroids possess high adipogenic capacity and acquire an adipose tissue-like extracellular matrix pattern *Tissue Eng. A* **26** 915–26
- [31] Datta P, Dey M, Ataie Z, Unutmaz D and Ozbolat I T 2020 3D bioprinting for reconstituting the cancer microenvironment *npj Precis. Oncol.* **4** 18
- [32] Hoarau-Vechot J, Rafii A, Touboul C and Pasquier J 2018 Halfway between 2D and animal models: are 3D cultures the ideal tool to study cancer-microenvironment interactions? *Int. J. Mol. Sci.* **19** 181
- [33] Albritton J L and Miller J S 2017 3D bioprinting: improving *in vitro* models of metastasis with heterogeneous tumor microenvironments *Dis. Models Mech.* **10** 3–14
- [34] Zhang Y S, Duchamp M, Oklu R, Ellisen L W, Langer R and Khademhosseini A 2016 Bioprinting the cancer microenvironment *ACS Biomater. Sci. Eng.* **2** 1710–21
- [35] Pati F, Ha D H, Jang J, Han H H, Rhie J W and Cho D W 2015 Biomimetic 3D tissue printing for soft tissue regeneration *Biomaterials* **62** 164–75
- [36] Gruene M, Pflaum M, Deiwick A, Koch L, Schlie S, Unger C, Wilhelmi M, Haverich A and Chichkov B N 2011 Adipogenic differentiation of laser-printed 3D tissue grafts consisting of human adipose-derived stem cells *Biofabrication* **3** 015005
- [37] Louis F, Piantino M, Liu H, Kang D H, Sowa Y, Kitano S and Matsusaki M 2021 Bioprinted vascularized mature adipose tissue with collagen microfibers for soft tissue regeneration *Cyborg Bionic Syst.* **2021** 1412542
- [38] Albrecht F B, Schmidt F F, Volz A C and Kluger P J 2022 Bioprinting of 3D adipose tissue models using a GelMA-bioink with human mature adipocytes or human adipose-derived stem cells *Gels* **8** 611
- [39] Zhu Y, Kruglikov I L, Akgul Y and Scherer P E 2019 Hyaluronan in adipogenesis, adipose tissue physiology and systemic metabolism *Matrix Biol.* **78–79** 284–91
- [40] Zhu Y C C and Scherer P E 2016 Hyaluronan in adipose tissue: beyond dermal filler and therapeutic carrier *Sci. Transl. Med.* **8** 323ps4
- [41] Guvendiren M, Lu H D and Burdick J A 2012 Shear-thinning hydrogels for biomedical applications *Soft Matter* **8** 260–72
- [42] Lim K S, Klotz B J, Lindberg G C J, Melchels F P W, Hooper G J, Malda J, Gawlitta D and Woodfield T B F 2019 Visible light cross-linking of gelatin hydrogels offers an enhanced cell microenvironment with improved light penetration depth *Macromol. Biosci.* **19** e1900098
- [43] Elkhoury K, Zuazola J and Vijayavenkataraman S 2023 Bioprinting the future using light: a review on photocrosslinking reactions, photoreactive groups, and photoinitiators *SLAS Technol.* **28** 142–51
- [44] Aguado B A, Mulyasmita W, Su J, Lampe K J and Heilshorn S C 2012 Improving viability of stem cells during syringe needle flow through the design of hydrogel cell carriers *Tissue Eng. A* **18** 806–15
- [45] Blaeser A, Duarte Campos D F, Puster U, Richtering W, Stevens M M and Fischer H 2016 Controlling shear stress in 3D bioprinting is a key factor to balance printing resolution and stem cell integrity *Adv. Healthcare Mater.* **5** 326–33
- [46] Foster A A, Marquardt L M and Heilshorn S C 2017 The diverse roles of hydrogel mechanics in injectable stem cell transplantation *Curr. Opin. Chem. Eng.* **15** 15–23
- [47] Lindsay C D, Roth J G, LeSavage B L and Heilshorn S C 2019 Bioprinting of stem cell expansion lattices *Acta Biomater.* **95** 225–35
- [48] Cidonio G, Glinka M, Dawson J I and Oreffo R O C 2019 The cell in the ink: improving biofabrication by printing stem cells for skeletal regenerative medicine *Biomaterials* **209** 10–24
- [49] Colle J, Blondeel P, De Bruyne A, Bochar S, Tytgat L, Vercruyse C, Van Vlierberghe S, Dubrue P and Declercq H 2020 Bioprinting predifferentiated adipose-derived mesenchymal stem cell spheroids with methacrylated gelatin ink for adipose tissue engineering *J. Mater. Sci., Mater. Med.* **31** 36
- [50] Zhou X, Zhang J, Lv W, Zhao C, Xia Y, Wu Y and Zhang Q 2022 The pleiotropic roles of adipocyte secretome in remodeling breast cancer *J. Exp. Clin. Cancer Res.* **41** 203
- [51] Fasshauer M and Bluher M 2015 Adipokines in health and disease *Trends Pharmacol. Sci.* **36** 461–70
- [52] Ouchi N, Parker J L, Lugus J J and Walsh K 2011 Adipokines in inflammation and metabolic disease *Nat. Rev. Immunol.* **11** 85–97
- [53] Kumar N, Zaman M H, Kim H D and Lauffenburger D A 2006 A high-throughput migration assay reveals HER2-mediated cell migration arising from increased directional persistence *Biophys. J.* **91** L32–4
- [54] Gorelik R and Gautreau A 2014 Quantitative and unbiased analysis of directional persistence in cell migration *Nat. Protocols* **9** 1931–43
- [55] Langer E M et al 2019 Modeling tumor phenotypes *in vitro* with three-dimensional bioprinting *Cell Rep.* **26** 608–23.e6
- [56] Hume R D, Berry R, Reichelt S, D'Angelo M, Gomm J, Cameron R E and Watson C J 2018 An engineered human adipose/collagen model for *in vitro* breast cancer cell migration studies *Tissue Eng. A* **24** 1309–19
- [57] Hume R D, Pensa S, Brown E J, Kreuzaler P A, Hitchcock J, Husmann A, Campbell J J, Lloyd-Thomas A O, Cameron R E

- and Watson C J 2018 Tumour cell invasiveness and response to chemotherapeutics in adipocyte invested 3D engineered anisotropic collagen scaffolds *Sci. Rep.* **8** 12658
- [58] Fujisaki K, Fujimoto H, Sangai T, Nagashima T, Sakakibara M, Shiina N, Kuroda M, Aoyagi Y and Miyazaki M 2015 Cancer-mediated adipose reversion promotes cancer cell migration via IL-6 and MCP-1 *Breast Cancer Res. Treat.* **150** 255–63
- [59] Dirat B *et al* 2011 Cancer-associated adipocytes exhibit an activated phenotype and contribute to breast cancer invasion *Cancer Res.* **71** 2455–65
- [60] Li R, Hebert J D, Lee T A, Xing H, Boussoimmier-Calleja A, Hynes R O, Lauffenburger D A and Kamm R D 2017 Macrophage-secreted TNFalpha and TGFbeta1 influence migration speed and persistence of cancer cells in 3D tissue culture via independent pathways *Cancer Res.* **77** 279–90